CHAPTER 2

Characterisation of a spontaneous parametric down-conversion source for spatially-entangled photon pairs

2.1 Introduction

Spontaneous parametric down-conversion (SPDC), in the older literature frequently referred to as parametric fluorescence or parametric scattering [72–74], is a second-order nonlinear optical process in which a high-frequency photon spontaneously splits in two lower-frequency photons, such that energy is conserved. It is thereby the inverse process of the more widely known up-conversion processes of second-harmonic generation (SHG) and sum-frequency generation (SFG), where two low-frequency beams are nonlinearly mixed to produce one high-frequency component [75, 76].

The process of SPDC has found common application in various fields of research. In the past, it has been used as a tool to measure the second-order nonlinear optical susceptibility tensor for a variety of materials [77–79]. An advantage of this method over more common methods based on SHG and SFG [80], lies in the fact that in SPDC the conversion efficiency is independent of the pump power, hence obviating the need for detailed knowledge of the pump beam's characteristics. SPDC is also the initiating process in optical parametric oscillators, as it generates the seed photons from which the coherent output builds up via parametric amplification [74, 81]. Owing to their large frequency tuning range, parametric oscillators are popular sources of tunable, narrowband light in a variety of fields, ranging from coherent anti-Stokes Raman spectroscopy [82] to continuous-variable quantum optics [83]. In recent years, SPDC has made its mark on the fields of quantum optics and quantum information, as a source of quantum states of light. In particular, it has become a standard instrument for the production of entangled photons [84–86], paving the way for such applications as quantum cryptography, quantum teleportation, quantum imaging, etc. [9, 11]. To date, SPDC remains an unparalleled source of entangled photon pairs in terms of brightness, reliability, and universality.

For the experimental work presented in this thesis, we exploit the process of SPDC for the creation of orbital-angular-momentum (OAM) entangled photon pairs. The efficiency of the

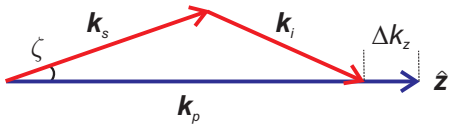

Figure 2.1: **Representation of the pump, signal, and idler wave vectors in SPDC.** The down-converted signal and idler wave vectors $\mathbf{k}_s$ and $\mathbf{k}_i$ point away from the pump wave vector $\mathbf{k}_p$ in such a way that transverse momentum is conserved. The longitudinal mismatch is denoted as Δk_z.

conversion process depends, amongst others, strongly on the wave-vector mismatch $\Delta\mathbf{k}$ between the pump and down-converted photons travelling through the nonlinear medium. This sensitivity on the mismatch sets limits to the spatial distribution in which the down-converted light is emitted. Consequently, when studying spatial (quantum) correlations between the photons in a pair, it is important to have a full understanding of the spatial structure of the SPDC source, and the dependence thereof on phase matching.

In the present Chapter, we present the results of an experimental characterisation of our SPDC source. We study the spatial structure of the down-converted light by imaging the far field of the light emitted from the nonlinear crystal and investigate the dependence of the emission on phase matching. The experimental data are used to estimate the number of entangled modes emitted by our source, characterised by the Schmidt number [50, 87]. This number serves as a benchmark for the work in the ensuing Chapters of this thesis, substantiating some useful assumptions we make regarding the spatial structure of the entanglement.

2.2 Phase matching

The process of SPDC does not exchange energy with the nonlinear crystal, and, consequently, the energy of a pump photon $\hbar\omega_p$ reappears as the sum of the energies of the two generated photons:

$$\omega_p = \omega_s + \omega_i. \tag{2.1}$$

Here, ω_s and ω_i refer to the frequencies of the generated photons, traditionally named signal (s) for the high-frequency photon and idler (i) for the low-frequency partner.

In the limit that the transverse cross section of the nonlinear crystal is much larger than that of the pump beam, the setup is invariant to translations in the plane of the crystal. Consequently, the transverse component of the wave vector has to be conserved. This implies that the signal and idler photons in a pair have equal but opposite transverse wave vectors. Because of the finite length of the crystal, the longitudinal component of the wave vector does not need to be conserved; the ensuing wave-vector mismatch between the pump, idler, and signal waves is given by (see Fig. 2.1)

$$\Delta\mathbf{k} = \Delta k_z = k_{p,z} - k_{s,z} - k_{i,z}. \tag{2.2}$$

Here, $k_j = 2\pi n_j/\lambda_j$, with n_j the (wavelength-dependent) refractive index of the nonlinear medium and λ_j the wavelength of the light.

The efficiency of any nonlinear optical process depends strongly on this wave-vector mismatch. The emission is brightest if the various fields are coherent over the full length of the

crystal. For that reason, nonlinear optical processes are preferably operated under phase-matched conditions, *viz.*, $\Delta\mathbf{k} \simeq 0$.

Dispersion in the nonlinear material between pump, signal, and idler waves hereby plays an inhibiting role and should be eliminated. This can be achieved with the use of birefringent nonlinear crystals. In such crystals perfect phase matching can be attained by appropriately orienting the crystal axes, and the wave vectors and polarization vectors of the input fields. However, it is often the case that the strongest nonlinearities cannot be addressed in this manner. Consequently, considerable effort has been devoted to develop materials that combine perfect phase matching with a strong nonlinear response, resulting in a multitude of quasi-phase-matched and periodically-poled materials [88, 89].

In up-conversion processes such as SHG and SFG, the concept of phase matching has a clear experimental significance: it simply determines the net power of the up-converted beam. This is due to the fact that the two fixed input waves impose quite a stringent condition on the frequency and directionality of the generated harmonic. When perfect phase matching is not met, the emitted radiation is much weaker and modulates rapidly as a function of the phase mismatch. This behaviour was first reported by Maker *et al.*, who investigated SHG from a crystalline quartz sample [90]. Although quartz does not allow for perfect phase matching, they observed a weak second-harmonic signal that varied in power with the orientation of the crystal, *i.e.*, with $\Delta\mathbf{k}$. Nowadays, this modulation goes by the name of "Maker fringes" [91, 92].

In SPDC, the system has more freedom to obey the phase-matching condition, and a change of the crystal orientation does not necessarily lead to an increase or decrease in the radiated power. Rather, it may result in a directional and/or frequency redistribution of the emitted radiation, since Eqs. (2.1) and (2.2) together allow for a certain freedom in the frequencies and directionalities of the generated photons. This flexibility lies at the heart of the wide tuning range of parametric oscillators. Nevertheless, power variations equivalent to those encountered in SHG and SFG appear when the output power is measured within a narrow spectral bandwidth and within a well-defined range of wave vectors, that is, if one is selective regarding the frequency-mode and spatial-mode structure of the SPDC light.

Let us study the spatial structure of the SPDC emission in closer detail. In a plane-wave description, the down-converted field emanating from a non-linear crystal of length L is of the general form

$$E \propto \int_0^L e^{i\Delta k_z z} dz \propto \frac{\sin(\frac{1}{2}\Delta k_z L)}{\frac{1}{2}\Delta k_z L} L. \tag{2.3}$$

This function is strongly peaked around $\Delta k_z = 0$, corresponding to perfect phase matching.

To find the exact spatial distribution of this phase-matched emission, we should take into account the polarization dependence of the problem. Phase matching in SPDC can usually be accomplished in two configurations, known as Type-I and Type-II phase matching. In the latter case, the polarization of the generated signal and idler waves are mutually orthogonal, causing them to experience different refractive indices inside the birefringent nonlinear crystal. Consequently, signal and idler emerge in different directions, in the form of two cones that can be tuned to intersect. Examples of such Type-II rings have appeared on the cover of various books and magazines [11] in the wake of advances in quantum information processing. By selecting light from the intersections of the rings, this configuration serves as a source of

polarization entangled photon pairs [86]. In our pursuit to create OAM-entangled photons, on the contrary, we have chosen to use Type-I phase matching. In this configuration, signal and idler photons have the same polarization and emerge in a single cone coaxial with the pump beam axis. The aperture of the cone can be widened or shrunk by tuning the phase-matching. Of particular interest is the situation that the cone is contracted to the point that the emission is beam-like. This relieves the need of apertures and the accompanying truncation of spatial modes.

Equation (2.3) shows that the strength of the generated field is proportional to the crystal length L, while the width of the phase-matched cone is inversely proportional to L. Away from perfect phase matching, emission is fully inhibited whenever $\Delta k_z L$ equals a multiple of 2π, but revives weakly in between these nodes. These fringes constitute the SPDC analogy of Maker's observation; they have a spatial character and appear as rings around the perfectly phase-matched emission cone, somewhat reminiscent of an Airy diffraction pattern.

In the following Section, we will present experimental data of the spatial structure of the SPDC emission from a Type-I source.

2.3 Experimental results

In our experiment, we use a BBO crystal (β-barium borate, β-BaB_2O_4) that allows for Type-I phase matching by angle tuning of the crystal. Figure 2.2 shows a diagram of our experimental setup. The crystal of length 1 mm is pumped by a weakly focused (waist $w_0 = 250$ μm) Kr^+ laser beam of 100 mW power at a wavelength of $\lambda = 413$ nm. The pump beam is polarised along the extraordinary crystal axis, whereas the signal and idler beams are polarised along the ordinary axis. The phase mismatch can then be written as

$$\Delta k_z = 2\pi \left[\frac{n_e(\lambda_p, \Theta)}{\lambda_p} - \frac{n_o(\lambda_i)}{\lambda_i} - \frac{n_o(\lambda_s)}{\lambda_s} \right], \tag{2.4}$$

where the subscripts (o, e) denote the ordinary and extraordinary crystal axes, respectively. The extraordinary refractive index n_e depends on the tuning angle Θ between the direction of propagation and the optical axis of the crystal. The effective nonlinearity of BBO cut for Type-I collinear phase matching ($\Theta = 28.3°$) equals $d_{\text{eff}} = 1.9 \times 10^{-12}$ m/V [93]. Given the 1 mm crystal length, the total yield of the resulting down-converted light is only of the order of 10^4 photon pairs per second per spatial mode per nm bandwidth. This feeble signal must be filtered from the 100 mW pump beam ($\simeq 10^{17}$ photons per second), which is achieved by means of a blue laser mirror that reflects the pump beam. Additionally, an interference filter, centred around 826 nm with a 20 nm width, suppresses residual stray (pump) light and ensures that we detect only degenerate photon pairs with $\lambda_i \simeq \lambda_s$. We use an intensified CCD camera (Princeton PI-MAX) that is positioned in the Fourier plane of the crystal to detect the SPDC light. This far-field configuration enables us to characterise the angular emission profile of the degenerate down-converted light.

We will work close to the point where $\Delta k_z = 0$ and, furthermore, close to collinearity where signal and idler point in the same direction as the pump beam. Because $\lambda_i \simeq \lambda_s \simeq 2\lambda_p$, the phase mismatch can be approximated by

$$\Delta k_z \simeq |\mathbf{k}_p| - |\mathbf{k}_i| - |\mathbf{k}_s| + \tfrac{1}{2}(|\mathbf{k}_i| + |\mathbf{k}_s|)\zeta^2, \tag{2.5}$$

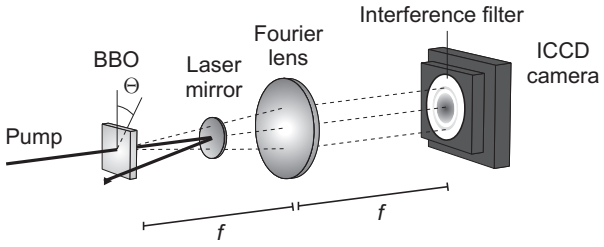

Figure 2.2: **Experimental Setup.** A 100 mW laser beam pumps a 1 mm nonlinear BBO crystal, cut for Type-I phase matching, at 413 nm. The pump beam is removed from the down-converted light by means of a blue laser mirror. A 826±10 nm interference filter selects frequency-degenerate SPDC light ($\lambda_i \simeq \lambda_s$), and the far-field emission profile is recorded by means of an intensified CCD camera.

where ζ is the angle between $\mathbf{k}_p$ and either $\mathbf{k}_i$ or $\mathbf{k}_s$ inside the crystal. Note that in the case of exact degeneracy and collinearity, only the term depending on ζ survives.

We have recorded far-field spatial distributions of the down-converted light for various tuning angles of the crystal. Figures 2.3(a)-(c) give three examples for different phase matching conditions (see below). These intensity profiles are plotted on a logarithmic false-colour scale in order to increase the visual contrast. We observe patterns of concentric rings of diminishing intensity. The bright ring stems from emission that obeys the phase matching condition $\Delta k_z = 0$. As discussed in the previous Section, the emission cone can be opened (see Fig. 2.3(a)) or closed (see Fig. 2.3(b)), depending on the tuning angle of the nonlinear crystal. In Fig. 2.3(c), the phase-matched ring has shrunk to a single spot, corresponding to collinear phase matching. Tilting the crystal even further will take it beyond perfect phase matching, and bright emission will no longer be possible. The fainter rings on the inside and outside of the phase-matched emission ring represent the subsidiary maxima of Eq. (2.3) and manifest a spatial variant of Maker's fringes. As the intensity drops rapidly with increasing wave-vector mismatch, at most two higher-order SPDC rings can be observed, given the background noise level. Although - with a little imagination - a hint of non-phase-matched emission rings may be discerned in observations from Refs. [94, 95], their appearance hasn't been discussed elsewhere. In the footsteps of the work discussed here, a high-quality spatial analysis of SPDC emission was presented in Ref. [96], using a 600 times brighter periodically-poled KTP (Potassium Titanyl Phosphate) source.

Let us compare our experimental results to the field distribution described by Eq. (2.3). Using Eq. (2.5), the intensity profile can be written as

$$I \propto |E|^2 \propto \left[\frac{\sin(\varphi + c\xi^2)}{\varphi + c\xi^2}\right]^2, \tag{2.6}$$

where the variable ξ is the external emission angle in air, given by $\xi^2 = (n\zeta)^2 = \xi_x^2 + \xi_y^2$. The factor $c = (|\mathbf{k}_s| + |\mathbf{k}_i|)L/(2n)^2$ is a constant, equal to $c = 2.29 \times 10^3$ for our experimental parameters (crystal length 1 mm and refractive index $n = 1.66$ for both signal and idler). The parameter $\varphi = (|\mathbf{k}_p| - |\mathbf{k}_s| - |\mathbf{k}_i|)L/2$ determines the opening angle of the emission cone, *i.e.*, it is a measure of the non-collinearity of the process. The radius of the perfectly phase-matched

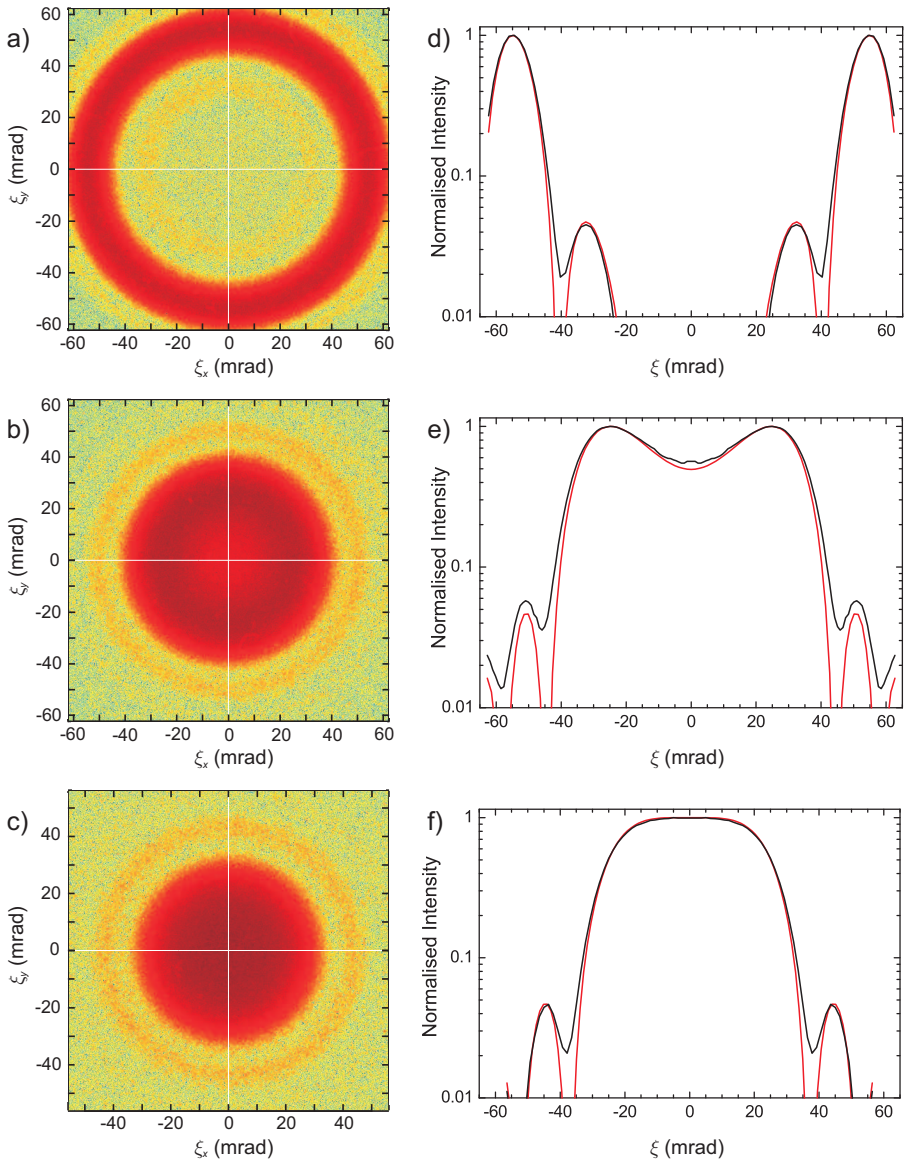

Figure 2.3: **Experimental emission profiles of our Type-I SPDC source. (a)**-**(c)** Narrow-band far-field spatial profiles around λ = 826 nm for various values of the phase-matching (see text), plotted on a logarithmic scale. **(d)**-**(f)** Their respective cross sections (black curves) were azimuthally averaged and fit to Eq. 2.6 (red curves). Graphs **(c)** and **(f)** correspond to collinear alignment.

SPDC ring in the Fourier plane is given by $\xi_R = \sqrt{-\varphi/c}$. The phase-matched cone is open for $\varphi < 0$, with collinearity occurring at $\varphi = 0$. For $\varphi > 0$ perfect phase matching is no longer possible.

Figures 2.3(d)-(f) show the cross sections (solid curves) of Figs. 2.3(a)-(c), respectively. These cross sections, obtained after careful determination of the profile centres, were azimuthally averaged and normalized to maximum intensity. The dashed curves represent the theoretical prescription from Eq. (2.6), where only the "non-collinearity" φ was left as a fitting parameter. From these fits, we found $\varphi = -6.90$ rad and $\varphi = -1.40$ rad for Fig. 2.3(d) and 2.3(e), respectively. For Fig. 2.3(f) we obtained $\varphi = -0.05$ rad, in correspondence with the statement that $\varphi \to 0$ at collinearity. Similar results were obtained when leaving c as a second fitting parameter.

2.4 Estimate of the number of spatially entangled modes

The intensity measurements in Fig. 2.3 of the parametric fluorescence from the nonlinear crystal are in itself classical. Between the signal and idler photons, however, exist spatial correlations that are essentially of quantum nature. This has been confirmed and exploited in numerous experiments [40, 44, 47, 97], and here, we will adopt a quantum description of the emission without further justification.

As argued in Section 2.2, signal and idler photons in a pair have equal but opposite transverse momenta. Both signal and idler photons are individually in a superposition of spatial modes, in such a way that their composite state is pure and entangled. In view of our work in the coming Chapters, we will write this entangled state in a cylindrical basis, namely [33, 34],

$$|\Psi\rangle = \sum_{m,p} c_{mp} |m, p\rangle_A |-m, p\rangle_B. \tag{2.7}$$

Here, $|m, p\rangle_A$ ($|m, p\rangle_B$) represents a signal (idler) spatial mode containing one photon, with $p \geq 0$ a radial and $m = -\infty, \ldots, \infty$ an azimuthal integer mode index. The entangled state of Eq. (2.7) is represented in its diagonalised Schmidt decomposition, meaning that it is written as a sum over biorthogonal product states (and the modes of photons A and B thus carry the same indices m and p) [98]. The complex expansion coefficients c_{mp} obey the normalization requirement $\sum_{m,p} |c_{mp}|^2 = 1$.

In general, it is not a trivial task to find the mode functions $f_{m,p}(\mathbf{r}) = \langle \mathbf{r}|m, p\rangle$ for down-conversion systems as those described in Section 2.2. Approaches to do so can be found in Refs. [33, 87, 99]. Due to the cylindrical symmetry in Type-I phase matching, however, the azimuthal content is readily obtained; the eigenmodes of rotation around the symmetry axis are of the form $e^{im\theta}$, and thus $f_{m,p}(\mathbf{r}) = f_{m,p}(r)e^{im\theta}$, with θ the azimuthal angle. Modes of this form are also eigenmodes of the OAM operator $\hat{L}_z = -i\partial/\partial\theta$ [100], and $|m, p\rangle$ thus represents a spatial mode containing one photon with OAM $m\hbar$. Note that conservation of OAM ($m_A = -m_B$) was already incorporated in Eq. (2.7).

The coming Chapters will predominantly deal with angular entanglement. Hence, we are particularly interested in the azimuthal m-content of the state. Let us therefore inspect the angular modal spectrum of Eq. (2.7), also known as the *spiral bandwidth* [33, 35]. This quantity

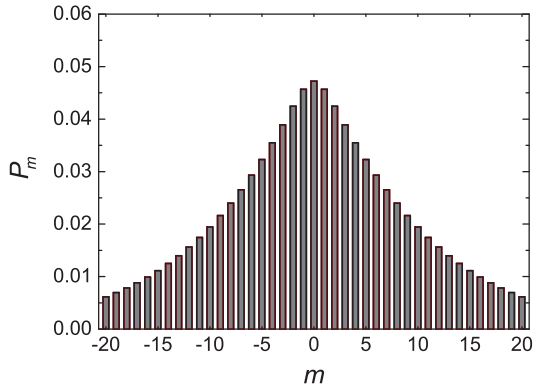

Figure 2.4: **Azimuthal probability distribution of the generated state.** Spiral content $P_m = \sum_p |c_{mp}|^2$ of the Schmidt decomposition (see Eq. (2.7)), calculated for our system. We assumed collinear phase matching and used the experimental parameters as given in Section 2.3.

gives the OAM probability distribution P_m, obtained by summing over the radial part,

$$P_m = \sum_p |c_{mp}|^2. \tag{2.8}$$

Figure 2.4 shows the spiral bandwidth of our source, calculated for collinear phase matching and the experimental values for the pump beam waist w_0 and the crystal length L mentioned in Section 2.3 [35]. We observe a broad spectrum that is symmetric around $m = 0$, which is a consequence of the fact that our Gaussian pump has $m = 0$. The histogram has a considerable width with long tails extending to high m numbers. Obviously, however, the modes in the superposition carry unequal weights.

In principle, the number of entangled modes in Eq. (2.7) can be infinite. However, it is natural to take the relative weight of the modes into account and to define an *effective* number of entangled modes. This is done by the so-called Schmidt number, given by [50, 87]

$$K = \frac{1}{\sum_{m,p} |c_{mp}|^4}, \tag{2.9}$$

For the case that one is only interested in the azimuthal m-content (*i.e.*, the spiral bandwidth) of the state, it can be derived that [34]

$$K_{\mathrm{az}} = \frac{1}{\sum_m P_m^2} \simeq 2\sqrt{K}. \tag{2.10}$$

The Schmidt number is commonly used as a meaningful quantifier of (high-dimensional) entanglement [87].

In principle, if one manages to construct the Schmidt basis $\{|m, p\rangle\}$, the Schmidt decomposition as given in Eq. (2.7) allows to calculate K theoretically, provided one computes enough terms in the expansion. However, in many cases this is not so easy. Moreover, this procedure does not provide a clear way to determine K experimentally. To this end, Refs. [87] and [101]

presented two independent methods to measure the Schmidt number experimentally. In the following, we use these methods to estimate the Schmidt number for our experimental configuration.

In Ref. [87], Law and Eberly provided an approximation in terms of the ratio of the far-field beam widths σ_{pump} and σ_{SPDC} of the pump and SPDC emission, respectively,

$$K \simeq \frac{1}{4}\left(\frac{\sigma_{pump}}{\sigma_{SPDC}} + \frac{\sigma_{SPDC}}{\sigma_{pump}}\right)^2, \tag{2.11}$$

where $\sigma_{pump} = 2/w_0$ and $\sigma_{SPDC} = \sqrt{4k_p/L}$. Implicit to this result are the assumption of collinear phase matching and the approximation of Eq. (2.6) by a Gaussian of width σ_{SPDC}. Equation (2.11) constitutes in fact a lower limit to K [87]. Filling in the relevant experimental numbers for the pump beam waist, wave number, and crystal length, we arrive at $K = 395$ (and $K_{\mathrm{az}} = 40$). Evidently, the widths σ_{pump} and σ_{SPDC} can also be estimated experimentally. In Fig. 2.5 we reproduced the far-field intensity profile of the source for nearly collinear phase-matching. The inset shows the Gaussian profile of the pump beam in the same plane.* The scale of the inset is magnified by a factor of five compared to the main graph. We observe that the pump beam is much more compact than the generated SPDC light. We made a rough estimate of the angular widths by simply taking the full width at half maximum and arrived at $\sigma_{SPDC} = 48$ mrad and $\sigma_{pump} = 1.2$ mrad. Equation (2.11) thus yields $K = 385$ ($K_{\mathrm{az}} = 39$), in good agreement with the calculation presented above. As stated earlier, this result based on Eq. (2.11) constitutes a lower boundary to the Schmidt number.

Recently, a more accurate method to measure the Schmidt number was demonstrated in Ref. [101]. Using concepts from classical coherence theory, this method takes into account the detailed spatial structure of the two-photon field. It yields the Schmidt number in terms of the spatial degree of coherence of field,

$$K \simeq \frac{1}{\lambda^2}\frac{\left[\int I_{NF}(\mathbf{r})d\mathbf{r}\right]^2}{\int I_{NF}^2(\mathbf{r})d\mathbf{r}}\frac{\left[\int I_{FF}(\boldsymbol{\xi})d\boldsymbol{\xi}\right]^2}{\int I_{FF}^2(\boldsymbol{\xi})d\boldsymbol{\xi}} \tag{2.12}$$

where $I_{NF}(\mathbf{r})$ and $I_{FF}(\boldsymbol{\xi})$ are the spatial intensity profiles of the down-converted light measured in the near field and far field of the nonlinear crystal, respectively. In the near field, the SPDC profile simply adopts the Gaussian profile of the pump beam (see inset Fig. 2.5). In the far field, the profile shows the concentric structure as presented in Fig. 2.5. Based on the theoretical descriptions for the near field and far field (see Eq. (2.6)), we calculate the Schmidt number to be $K = 930$. Using the experimental data from Fig. 2.5, we obtain an experimental value of $K = 850$, probably being a slight underestimate due to the noise floor of the measurement.

In summary, the calculated Schmidt number based on Eq. (2.12) is confirmed by our experiment. Moreover, this result is consistent with the lower bound according to Eq. (2.11).

* For experimental convenience, in reality we did not use the bright pump beam itself for this purpose, but an auxiliary beam that was mode matched to it to a very high degree.

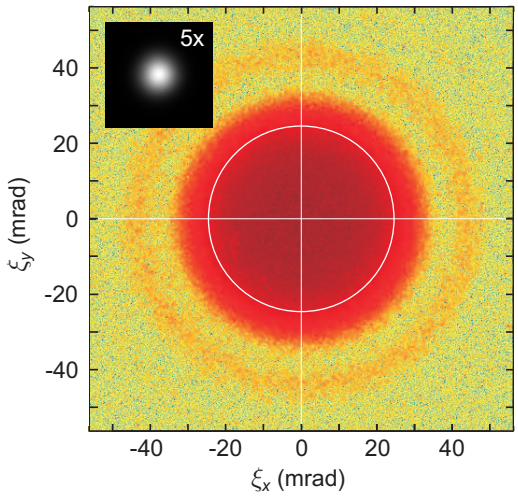

Figure 2.5: **Experimental determination of the Schmidt number.** Narrow-band far-field intensity profile of the SPDC light for collinear phase matching, reprinted from Fig. 2.3(c). The circle indicates the full-width-at-half-maximum intensity level of the central spot. Inset: size of the Gaussian pump beam in the same plane, plotted with five times magnification for comparison. A rough estimate of the Schmidt number is obtained by taking the ratios of the two beam sizes (see Eq. (2.11)), yielding $K = 385$. A more careful analysis based on Eq. (2.12) yields $K = 850$.

2.5 Conclusions

We have characterised the parametric fluorescence from a Type-I SPDC source, which we will employ in the coming Chapters to create OAM-entangled photon pairs. The emission profiles were spatially analysed, and the influence of phase matching on the emission cone aperture was studied. Apart from dominant phase-matched emission, we observed secondary non-phase-matched emission rings, which are a spatial analogy of the well-known Maker fringes exhibited in second-harmonic generation and sum-frequency generation.

Furthermore, we computed the spiral bandwidth of the OAM-entangled modes and estimated the Schmidt number of the generated two-photon field to be 850. The corresponding azimuthal Schmidt number is approximately equal to 60, a number that is sufficiently large for the purpose of our experiments.